Bayesian calibration for Lamb wave propagation on a composite plate using a machine learning surrogate model

Leonardo de Paula S. Ferreira[a], Rafael de O. Teloli[b], Samuel da Silva[c], Eloi Figueiredo[d,e], Ionut D. Moldovan[d,e], Nuno Maia[f], Carlos Alberto Cimini Jr. [1a]

[a] *UFMG – Universidade Federal de Minas Gerais, Faculdade de Engenharia, Departamento de Engenharia de Estruturas, Av. Pres. Antonio Carlos, 6627, Belo Horizonte, 31270-901, MG, Brazil*
[b] *SUPMICROTECH, CNRS, FEMTO-ST, Applied Mechanics Department, 26 Rue de l'Épitaphe, Besançon, 25000, France*
[c] *UNESP – Universidade Estadual Paulista, Faculdade de Engenharia de Ilha Solteira, Departamento de Engenharia Mecânica, Av. Brasil, 56, Ilha Solteira, 15385-000, SP, Brazil*
[d] *Lusófona University, Faculty of Engineering, Campo Grande, 376, Lisboa, 1749-024, Portugal*
[e] *CERIS, Instituto Superior Técnico, University of Lisbon, Av. Rovisco Pais, Lisboa, 1749-024, Portugal*
[f] *IDMEC, Instituto Superior Técnico, University of Lisbon, Av. Rovisco Pais, Lisboa, 1049-001, Portugal*

Abstract

This paper presents a new framework for stochastic updating of a finite element model for a composite plate, considering the influence of temperature on Lamb wave propagation. The framework involves deterministic updating to optimize mechanical properties and stochastic updating to derive probability density functions for key parameters. It utilizes sensitivity analysis and Bayesian inference with Markov-Chain Monte Carlo simulations and the Metropolis-Hastings sampling algorithm. This paper proposes a machine learning surrogate model based on artificial neural networks to improve computational efficiency. This surrogate modeling approach allows parallelized Monte Carlo simulations, reducing updating time significantly without compromising the accuracy of the resulting probability density functions for model parameters. These advancements show a promising way to enhance composite plate modeling and Lamb wave propagation studies, providing a more efficient and accurate approach to verify and validate finite element models with potential applications in engineering simulations.

Keywords: Lamb wave, Bayesian calibration, Sobol indices, Surrogate model, operational and environmental variations

1. Introduction

Lamb waves are ultrasonic-guided elastic waves widely used for structural health monitoring (SHM) and assessing plate-like structures in various applications. Due to their ability to travel long distances, Lamb waves find applications in local inspections (fatigue [1], corrosion [2], bonded joints [3]) and large-scale structures such as aerospace components [4]. This work focuses on Lamb wave propagation in composite structures [5], facing challenges from material heterogeneity and the influence of temperature and humidity on physical properties [6, 7].

---

[1] Corresponding author: carlos.cimini@gmail.com

Guided wave propagation simulation in composite structures is an active research area with various methods available, including semi-empirical and numerical [8, 9]. Among numerical methods, the finite element (FE) method stands out for its accurate representation of wavefront propagation in complex structures [10]. However, high-frequency simulations or modeling small features require very fine mesh density, leading to computationally expensive models. To achieve a desirable degree of fidelity and consider environmental variations, FE models must be updated with experimental data [11].

Stochastic updating approaches, like Bayesian updating [12], consider uncertainties during calibration and are widely used in various works [13, 14, 15, 16]. Previous studies have applied Bayesian inference to composite structures subjected to Lamb wave excitation, using methods like Local Interaction Simulation Approach (LISA) and Wave and Finite Element (WFE) [17, 18]. However, the Bayesian inference process can be computationally expensive, necessitating surrogate modeling techniques [19, 20, 21, 22, 23, 24, 25].

This paper proposes a framework for stochastic calibration of a FE model for Lamb wave propagation in composite structures, including temperature effects. It combines deterministic and stochastic updating, utilizing a modified least-squares method and Bayesian inference with Markov-chain Monte Carlo (MCMC) simulations [26]. To reduce computational time, this paper proposes an approach consisting of a machine learning a surrogate model based on artificial neural networks (ANNs), which can be trained using parallelized Monte Carlo simulations. The proposed approach efficiently updates the FE model for Lamb wave applications, considering temperature influences [17, 18].

This work enhances Lamb wave research in composite structures subjected to environmental variations, providing a systematic framework incorporating experimental uncertainty into FE models. The ANN surrogate model accelerates updating, maintaining accuracy in the resulting probability density functions for model input parameters. The paper's structure includes sections on the proposed framework, experimental setup, model updating application, final remarks and future work directions.

2. Problem statement and methodology framework

As a novelty contribution, this paper presents a framework for applying Bayesian inference to obtain a stochastic FE model for Lamb wave propagation under varying temperature. Additionally, the work proposes the use of a machine learning surrogate model based on ANN to considerably reduce the time required for the MCMC rounds. The work also evaluates the impact of the surrogate model on the posterior distribution sampled by the MCMC, along with database size and simulation time for training the surrogate model.

The proposed framework for stochastic calibration of a FE model for Lamb wave propagation on a composite plate is performed for multiple temperatures, aiming to construct a model capable of emulating the whole experimental dataset. The framework lays its foundation on the following assumptions and considerations:

1. The database made available by da Silva et al. [27] is used as an experimental setup, and it is considered that no material property is known *a priori*.
2. All effects imposed by temperature on measured signals are incorporated at the material level.
3. A set of material properties is obtained among various possibilities using a deterministic updating procedure with a modified version of the least-squares method [28]. The deterministic version of model parameters provides the necessary information for the stochastic updating procedure.
4. A sensitivity analysis using Sobol indices to identify the key parameters that significantly impact the model results and should therefore be included in the Bayesian inference process.
5. A Bayesian inference process using MCMC simulations and the Metropolis-Hastings sampling algorithm is used to sample posterior probability functions from uniform prior distributions.
6. The classical FE model-based approach is replaced by a machine learning surrogate model approach based on neural networks to reduce simulation time.

The complete strategy is presented in Fig. 1, and the underlying theoretical foundations are discussed in the subsequent subsections.

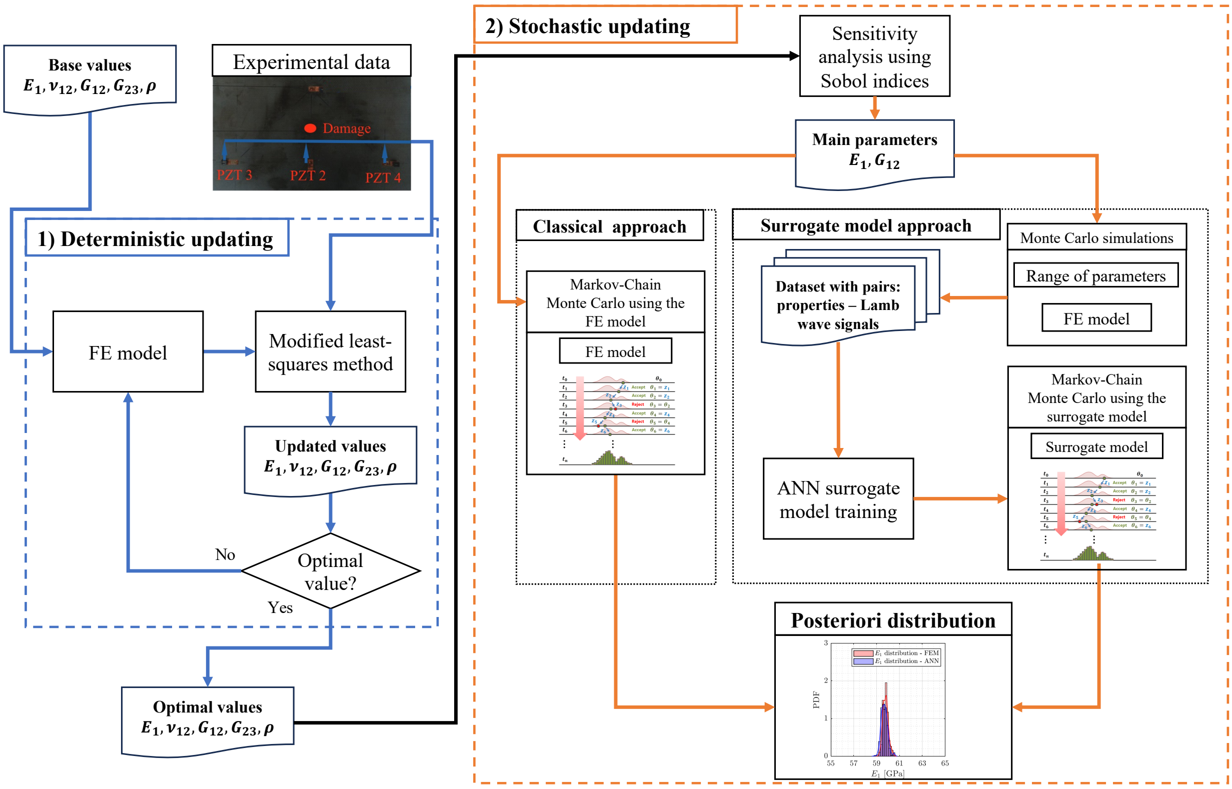

Figure 1: Proposed framework with deterministic and stochastic updating. MCMC illustration adapted from Jin et al. [29].

2.1. Deterministic updating procedure

This work uses a modified version of the least-squares method to perform a deterministic updating of input parameters. The method formulation is presented by Bud et al. [28], and it is a multi-loss optimization technique that aims to minimize multiple loss functions calculated from the model outputs. To achieve this objective, the impact of each input on the loss functions is linearized, and the numerical calculation of partial derivatives concerning each parameter is performed. Three residuals are established to measure the discrepancy between experimental and model signals. Note that although the equations presented are continuous, they are implemented using discrete numerical computations.

The first residual evaluates the squared norm of the difference between the experimental and numerical signals. This residual can quantify differences in amplitude and phase between the signals, and it is calculated according to the equation:

$$R_{\mathrm{NORM}} = \frac{\displaystyle\int_{t_1}^{t_2} [y(t) - x(t)]^2 dt}{\displaystyle\int_{t_1}^{t_2} x(t)^2 dt}. \tag{1}$$

where $x(t)$ is the experimental signal and $y(t)$ is the numerical signal.

The second residue is based on the cross-correlation between the signals, and it is calculated as:

$$R_{\mathrm{XCOR}} = 1 - r_{xy}, \tag{2}$$

where r_{xy} is the cross-correlation between the input signals and the signal with zero delays. This measure is only sensitive to changes in the shape and frequency of the signal, which is one of its main advantages. The third residual is the difference between the power spectra of the signals. This index is particularly useful for detecting delays and frequency shifts in the signals, and it is calculated as follows:

$$R_{\mathrm{PSD}} = \frac{\displaystyle\int_{f_1}^{f_2} [Y(f) - X(f)]^2 df}{\displaystyle\int_{f_1}^{f_2} X(f)^2 df}. \tag{3}$$

where $X(f)$ is the power spectra density of the experimental signal and $Y(f)$ is the the power spectra density of the numerical signal.

The final residual is defined as the weighted sum of the individual residuals:

$$R_{\mathrm{TOTAL}} = k_1\ R_{\mathrm{NORM}} + k_2\ R_{\mathrm{XCOR}} + k_3\ R_{\mathrm{PSD}}. \tag{4}$$

where k_1, k_2, and k_3 are adjustable weights assigned to each residual. These weights allow for controlling the relative importance of each metric in the outcome of the least-squares method.

2.2. *Stochastic updating procedure*

2.2.1. *Sensitivity analysis*

Sensitivity analysis is conducted to discover the effects of model parameters, called random input variables, on quantities of interest that form the model response. Suppose the response of the mathematical model is given by:

$$Y = \mathcal{M}(\boldsymbol{\Theta}), \tag{5}$$

where $\boldsymbol{\Theta} = (\theta_1, \theta_2, \ldots, \theta_k)$ is the vector containing the k input variables, and Y is a scalar quantity. For simplification purposes, the input parameters are considered uniformly distributed with support $\pi(\boldsymbol{\Theta}) \sim \mathcal{U}(0, 1)$. The sensitivity analysis using Sobol indices considers the decomposition of the model's response Y in terms of increasing dimensions:

$$\begin{aligned} Y = \mathcal{M}_0 + \sum_{i=1}^{k} \mathcal{M}_i \left(\theta_i\right) + \sum_{i<j}^{k} \mathcal{M}_{ij} \left(\theta_i, \theta_j\right) + \ldots \\ + \mathcal{M}_{1\ldots k} \left(\theta_1 \ldots \theta_k\right), \end{aligned} \tag{6}$$

where the constant $\mathcal{M}_0$ corresponds to the mean value $E(Y)$ of the model output. The integral of each summation above has zero means, then all the terms in Eq. (6) hold the orthogonality property. Consequently, these terms can be calculated using the conditional expectations $\mathcal{M}_0$. Thus, the terms $\mathcal{M}_i(\theta_i)$ and $\mathcal{M}_{ij}(\theta_i, \theta_j)$ are the conditional mean values for the parameters i and ij $(i \neq j)$ [30], respectively:

$$\mathcal{M}_i(\theta_i) = \int_0^1 \cdots \int_0^1 \mathcal{M}\left(\boldsymbol{\Theta}\right) \, d\boldsymbol{\Theta}_{\sim i} - \mathcal{M}_0, \tag{7}$$

$$\begin{aligned} \mathcal{M}_{ij}(\theta_i, \theta_j) = \int_0^1 \cdots \int_0^1 \mathcal{M}\left(\boldsymbol{\Theta}\right) \, d\boldsymbol{\Theta}_{\sim ij} - \mathcal{M}_0 - \\ \mathcal{M}_i(\theta_i) - \mathcal{M}_j(\theta_j), \end{aligned} \tag{8}$$

where the notation $\sim i$ indicates that parameter θ_i is excluded. As the model response from Eq. (5) is also a random variable, the conditional expectation variance can be considered a summary measure of sensitivity. Thus, one can compute the first-order Sobol indices that quantify the additive effect of each input parameter separately on the total variance:

$$S_i = \frac{Var[\mathcal{M}_i(\theta_i)]}{Var[\mathcal{M}(\boldsymbol{\Theta})]}, \tag{9}$$

This first-order index represents each input parameter's main contribution to the model output variance [31]. The second-order Sobol indices that quantify the interaction effects between two input parameters are defined as:

$$S_{ij} = \frac{Var[\mathcal{M}_{ij}(\theta_i, \theta_j)]}{Var[\mathcal{M}(\boldsymbol{\Theta})]}. \tag{10}$$

In this work, the first-order Sobol indices are analyzed to evaluate the influence of each parameter, and their values are calculated through Monte Carlo simulations. For this, the UqLab framework has been used [32].

2.2.2. Bayesian inference

Physical systems have inherent variations, e.g., geometry, environmental conditions, material properties, etc. Thus, even the most complete data set cannot eliminate this uncertainty, so-called irreducible. To include this type of variability in the parameters of the computational model, this work adopts the Bayesian paradigm as a statistical inference tool for the model calibration problem. Two assumptions are introduced: (i) As the model parameters are random variables, a prior distribution $\pi(\mathbf{\Theta})$ for the set of input variables $\mathbf{\Theta}$ is proposed based on the deterministic model updating procedure; (ii) Bayes' theorem is employed to update the before a posterior distribution, gathering information from random data observations ($\mathscr{D}$). The posterior density function (PDF) $\pi(\mathbf{\Theta}|\mathscr{D})$ is given by:

$$\pi(\mathbf{\Theta}|\mathscr{D}) = \frac{\pi(\mathscr{D}|\mathbf{\Theta})\pi(\mathbf{\Theta})}{\pi(\mathscr{D})}, \tag{11}$$

in which $\pi(\mathscr{D}|\mathbf{\Theta})$ is the likelihood function, and the denominator $\pi(\mathscr{D})$ is the marginal likelihood: it is a normalization constant that guarantees the definition of a probability density function with integral equal to unity. By considering a uniform prior distribution, Eq. (11) is simplified to $\pi(\mathbf{\Theta}|\mathscr{D}) \propto \pi(\mathscr{D}|\mathbf{\Theta})$, i.e., the updated posterior PDF is proportional to the likelihood distribution.

Assuming that the model predictions $\mathcal{D}^{\mathcal{M}}(\mathbf{\Theta})$ are corrupted by an additive decorrelated Gaussian noise of zero mean and variance σ_ε^2, the analytical expression for the likelihood function is given by:

$$\pi(\mathcal{D}|\mathbf{\Theta}) \propto \exp\left(-\frac{1}{2}\frac{\left(\mathcal{D}-\mathcal{D}^{\mathcal{M}}(\mathbf{\Theta})\right)^T\left(\mathcal{D}-\mathcal{D}^{\mathcal{M}}(\mathbf{\Theta})\right)}{\sigma_\varepsilon^2}\right). \tag{12}$$

With T superscript meaning transpose operation. The MCMC/Metropolis-Hastings algorithm is considered to sample the posterior density function. The random variables $\mathbf{\Theta}$ are limited to the interval $[\mathbf{\Theta}_{\min}, \mathbf{\Theta}_{\max}]$, whose current state is symmetrically normalized as $\mathbf{\Theta}' = (1-\boldsymbol{x})\mathbf{\Theta}_{\min} + \boldsymbol{x}\mathbf{\Theta}_{\max}$; $\boldsymbol{x}$ is a random variable $\in [0,1]$ that represents generated candidates for the posterior distribution. These candidates are sampled from a normal distribution with standard deviation σ_p. This hyperparameter controls the random walk step to avoid the chain becoming static and, at the same time, to allow the parameter space to be properly explored. Therefore, σ_p is adjusted to obtain an acceptance rate of candidates $40 \sim 50$ %. Only 80% of the Monte Carlo simulations are considered in the final stationary Markov chain (burn-in of 20%).

3. Experimental application and FE model

3.1. Experimental setup

The experimental setup shown in Fig. 2 consists of a 500 x 500 x 2 mm^3 carbon fiber reinforced polymer (CFRP) plate with 10 layers of plain weave fibers. The plain weave fibers are oriented along the plate borders' directions. Four PbZrTi (Lead Zirconate Titanate - PZT) SMART Layers from Accelent Technologies, each with a diameter of 6.35 mm, are bonded to the plate using epoxy resin. PZT 1 is the actuator, while PZT 2, PZT 3, and PZT 4 are sensors. Due to the dispersive nature of Lamb waves, the experiments are performed with a uniform excitation frequency across all tests, targeting a specific segment of the Lamb wave frequency-thickness spectrum. When considering the multimodal characteristic of Lamb waves, Wang and Yuan [8] suggest that for a plate of this nature, excitation of higher-order modes (A1, S1, A2, etc.) is expected to occur above 500 kHz. Therefore, the excitation signal is a 5-cycle sinusoidal wave modulated by a Hanning window, with an amplitude of 35V and a central frequency of 250 kHz, aiming to excite only S0 and A0 modes . The output is recorded with a sampling frequency of 5 MHz over a 100 μs window using a NI USB 63533 from National Instruments and an oscilloscope DSO7034B from Keysight. A comprehensive exploration of this experimental setup is presented by França [33].

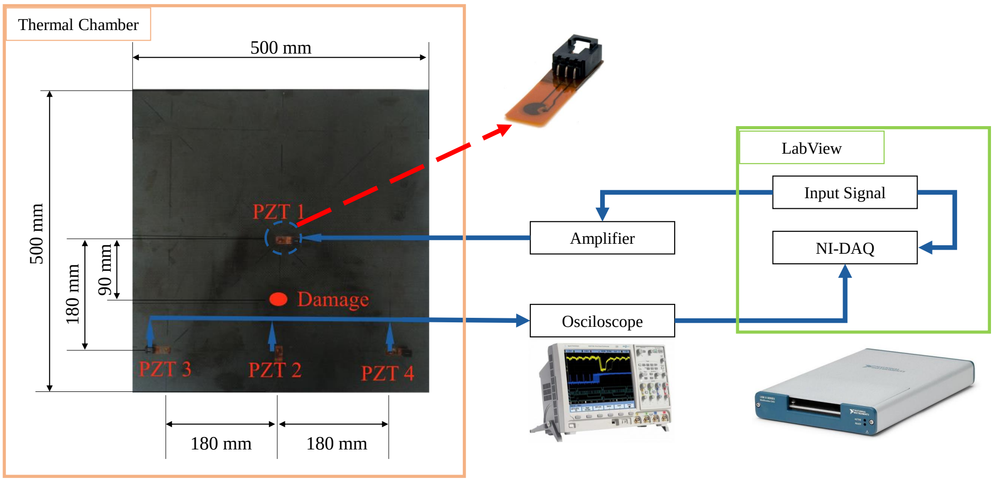

Figure 2: Experimental setup. Adapted from da Silva et al. [27]

Data acquisition is performed at controlled varying temperature ranging from 0°C to 60°C in increments of 10°C with a thermal chamber from Thermotron. For each temperature, 100 tests are repeated for statistical characterization. Figure 3 shows one experimental measurement for each temperature from 0°C to 60°C. The experiments are also performed in progressive damage scenarios [27], with mass added to the region shown in red in Fig. 2. However, the present study only considered the plate in its undamaged condition. The dataset is publicly available in the GitHub[2] repository CONCEPT: CarbON-epoxy CompositE PlaTe.

3.2. FE model

A FE model is implemented using ABAQUS/ Explicit. The plate is modeled using continuum shell elements (SCR8). These elements are designed to discretize a three-dimensional body rather than just representing a surface like traditional shell elements. Continuum shells have only displacement degrees of

---

[2] `https://github.com/shm-unesp/DATASET_PLATEUN01`

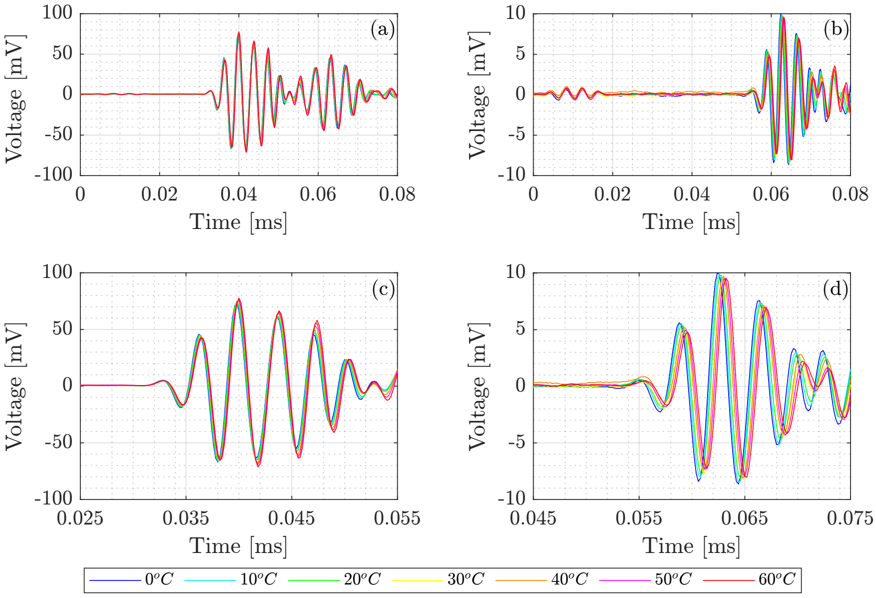

Figure 3: Experimental results for temperatures from 0°C to 60°C. (a) Complete signal PZT 2; (b) complete signal PZT 3; (c) zoom at first signal package PZT 2; and (d) zoom at first signal package PZT 3.

freedom, use linear interpolation, and include effects of transverse shear deformation and thickness change. Additionally, they are based on first-order composite theory and can be stacked to improve the accuracy of the through-thickness response.

The composite material is implemented in the FE model using ply-based properties. The layup is modeled as an orthotropic laminate property with three integration points per lamina. The discussion on the base properties and material considerations can be found in Section 4.1.

The spatial and temporal resolution of the model greatly affects the stability of the simulation. According to Moser [34], a spatial resolution of at least 20 nodes per wavelength is necessary to ensure stability. This can be written as $l_e = \lambda_{min}/20$, where λ_{min} is the minimum wavelength expected at the model and l_e is the characteristic length of the mesh. Additionally, to prevent numerical instability, the time step must be based on the maximum expected frequency in the simulation, with a recommended value of $\Delta t = 1/(20 f_{max})$, where Δt is the time step and f_{max} is the maximum frequency expected at the model. For an input frequency of 250 kHz, both these considerations result in a mesh with an element size of approximately 2 mm and a maximum time increment of 0.2 μs. However, further stability investigations of the model found that a time increment of 0.1 μs is needed to account for mesh irregularity around the PZT regions, ensure convergence, and keep the simulation time reasonable. The simulation window is set to 0.1 ms as this is the time necessary to capture the first two wave packets from Fig. 3.

Figure 4 presents the FE model. To facilitate the generation of a structured mesh for the entire plate, the plate is divided into several smaller rectangular regions, as shown in Fig. 4a. The area where the PZT actuators and sensors are attached to the plate is specifically modeled with a circular mesh. As proposed by Gresil et al. [35], the excitation signal is applied as eight self-balancing forces around this region, as depicted in Fig. 4b. To obtain the output signal, the integrated strain results within the sensor region are used and transformed to voltage as suggested by Sirohi and Chopra [36]. The region between PZTs 1 and 2 is modeled with a circular mesh to account for damage addition in future model versions. However, in the present work, this region has the same element, materials, and conditions as the rest of the plate.

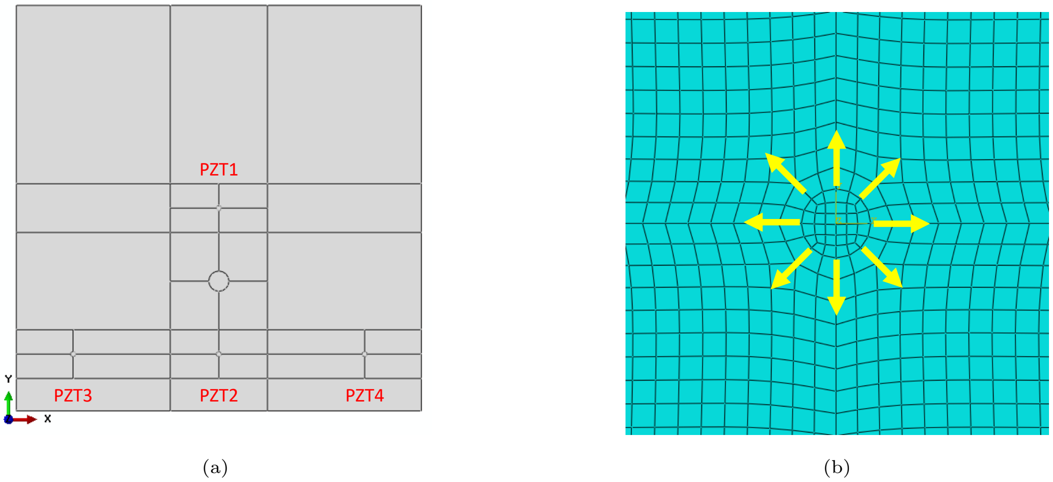

(a)

(b)

Figure 4: Finite element model. (a) Model partition for mesh generation and (b) PZT-1 showing excitation signal

The FE model is implemented using a series of Python routines that run within the Abaqus software, allowing for parametric simulation of the system. A code layer is also implemented using MATLAB and Windows command prompt, enabling direct control over Abaqus through the command line. This architecture made possible a complete automation of the pre-and post-processing steps of the simulation inside MATLAB's workspace. It also facilitated the usage of multiple machines to parallelize the Monte Carlo simulations.

4. Model updating framework: experimental application

4.1. Deterministic updating

The goal of the deterministic updating process is to bring the response signal of the FE model ($y(t)$) for sensors 2 and 3 as close as possible to the experimental results ($y_{\text{EXP}}(t)$), by adjusting the mechanical properties of the materials. The textcolorredFE model is symmetric concerning the horizontal and vertical axes, resulting in identical signals from PZTs 3 and 4. For this reason, only the PZT-3 signal is considered along with PZT-2 in the adjustment of mechanical properties. As the composite plate used in this work is obtained from a research project in partnership with a Brazilian aerospace company, which could not disclose the specific material or fabrication process used due to intellectual property agreements, the only information provided is that the plate is made of a prepreg aerospace-grade carbon fiber with 10 layers in a plain weave configuration [33]. Thus, the initial range of values for the mechanical properties had to be determined by literature review, as detailed below.

The mechanical behavior of the materials is modeled using the classical laminate theory, where each layer is considered an orthotropic material. As such, Young's modulus in two perpendicular directions in the plane (E_1 and E_2), Poisson's ratio (ν_{12}), shear moduli in and out of a plane (G_{12} and G_{23}, respectively), and density (ρ) had to be determined. It is necessary to establish an initial search range for these parameters. This range is determined based on information from the literature for plain weave carbon/epoxy systems, with the main sources being the Composite Materials Handbook (CMH) [37] and the work of Paiva et al. [38]. Table 1 presents the limits, initial and optimal values used for the following mechanical parameters: E_1, E_2, ν_{12}, G_{12} and ρ.

Table 1: Parameters limits and initial values utilized for the deterministic updating procedure, including resultant optimal values

Parameter	Min	Max	Initial Value	Optimal Value
E_1 [GPa]	60.0	80.0	70.0	61.2
E_2 [GPa]	60.0	80.0	70.0	61.2
ν_{12}	0.05	0.15	0.10	0.075
ρ $[Kg/m^3]$	1550	2250	1800	1620
G_{12} [GPa]	5.00	15.0	7.50	10.25
G_{23} [GPa]	4.00	6.00	5.00	5.00

As a simplification, it is assumed that the values of E_1 and E_2 for plain weave fibers are equal. The values presented in Tab. 1 are used as reference and adjusted using the iterative process based on least-squares method described in Bud et al. [28]. In each iteration, the model is initially simulated with the value of the properties from the former iteration. The residual between the experimental and model signals is calculated by Eq. (4). Next, each property is individually perturbed to determine the partial derivatives of the model response relative to inputs. The perturbation value is initially set to 5% and reduced over the optimization process to minimize system instability as the optimal values are approached. This process is repeated until the value of the residue converges. Only the first wave package in each channel is considered for the fitting. In the case of PZT 2, the second package shown in Fig. 3 represent edge reflections.

The oscillatory nature of the wave signal results in the residuals having multiple local extrema throughout the simulation range. For instance, if the simulated wave is one wavelength in advance or retard concerning the experimental data, the residual gives a local minimum. To mitigate this, the weights k_1, k_2, and k_3

in Eq. (4) are adjusted. Empirical testing has shown that weighting these parameters as 0.2, 0.4, and 0.3 can reduce the likelihood of becoming trapped in local minima, resulting in a better output signal. Also, intermediate solutions that give physically unrealistic properties are disregarded. Table 1 presents the initial and estimated values for the physical parameters of the material, whereas Fig. 5 compares the model results before and after the adjustment process. It is possible to observe that the adjustment process improved both the phase and the amplitude of the signals from PZTs 2 and 3.

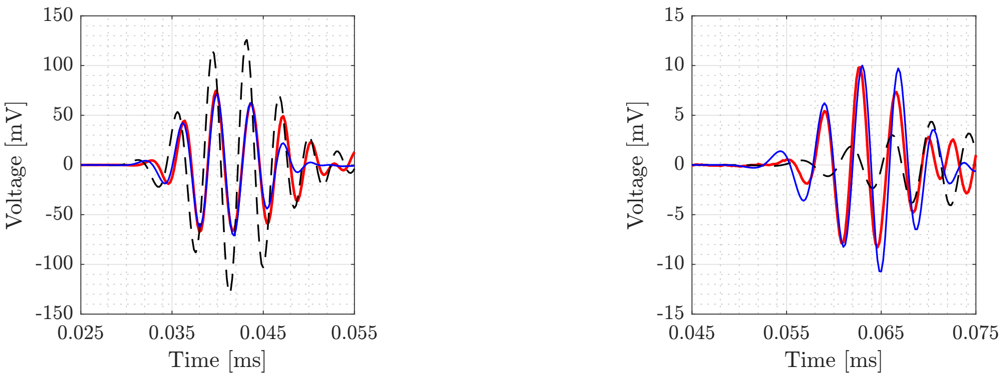

(a)

(b)

Figure 5: Comparison between experimental (—) and numerical results with initial (—) and optimal (—) parameters. (a) Signal from PZT 2; and (b) signal from PZT 3

Note that all parameters are well accommodated within the proposed ranges. For out-of-plane, the shear modulus G_{23} maintained its initial value even after optimization. Its variation within the established range does not influence the model performance - therefore, this parameter is kept fixed at 5 GPa in subsequent steps.

4.2. Stochastic updating

4.2.1. Sobol analysis

Following the deterministic adjustment, a sensitivity analysis is performed using Sobol indices to quantify each parameter's influence on the model's behavior. The parameters E_1, ν_{12}, G_{12}, and ρ are perturbed around the optimal deterministic values presented in Tab. 1. This perturbation is performed with 300 Monte Carlo simulations, in which model input parameters are sampled from an uniform distribution centered at the optimal values and bounded by ±20% limits. Two scores are defined to quantify the effect of the input parameters on the response of the model: the time of flight (TOF) and the maximum value of the envelope (AMP) of the first wave packet, as shown in Fig. 6a.

The first and second orders of Sobol indices are shown in Figs. 6b and 6c, respectively. Note that the parameters with the greatest impact on the results are E_1 and G_{12}, mainly affecting approximately 70% and 55% of the variance related to TOF and amplitude, respectively. The sensitivity analysis indicates that

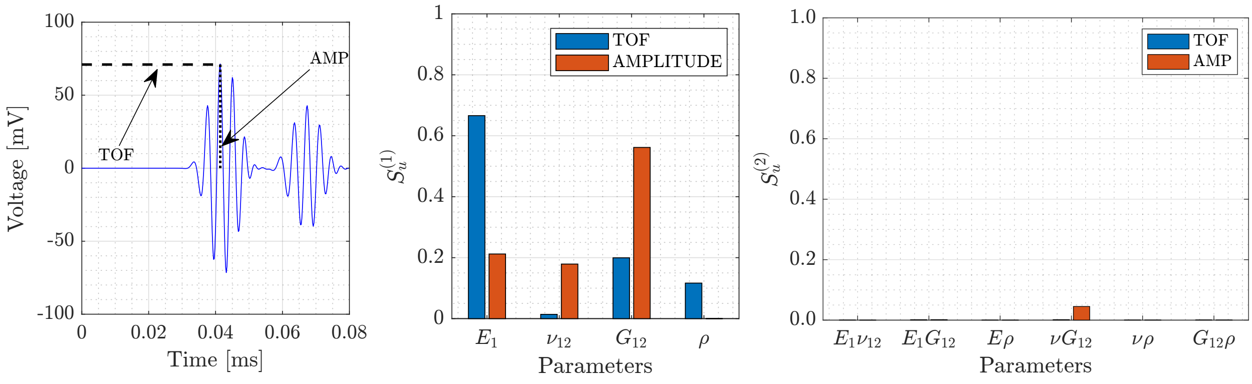

(a) (b) (c)

Figure 6: Sobol indices analysis. (a) TOF and AMP metrics; (b) first-order Sobol indices; and (c) second-order Sobol indices

ν and ρ have smaller influences when compared to E_1 and G_{12}. The combinations of parameters also have a negligible effect, with νG_{12} representing approximately 5% of the total variance related to the amplitude. Therefore, ν and G_{12} can be considered determined quantities, and their values are assigned based on the optimization results from Tab. 1, i.e., $\nu = 0.075$ and $\rho = 1620 kg/m^3$. The remaining parameters are considered undetermined, and updating their posterior probability distributions and gathering information from experimental data containing environmental variation is necessary. In summary, small intrinsic variations associated with uncertainties in the experimental data, which cause a slight change in the response pattern for the same test conditions, can influence the values identified for these parameters. Therefore, it demonstrates that in the presence of uncertainties in the experimental data, deterministic estimation of these parameters cannot be generalized - they must be treated as random variables.

4.2.2. ANN-based surrogate model for Lamb wave propagation

As MCMC simulations are very time-consuming, it is proposed to use a surrogate model to replace the FE model on random walking. Multiple techniques are available for surrogate modeling, such as the Gaussian process, PCE, or ANN. The authors chose to work with neural networks. The surrogate model in this study is a multilayer perceptron ANN, used as an interpolation model inside the parameters search space for the Bayesian inference process. The input layer consists of two neurons, representing the two random variables E_1 and G_{12}, used as input to the surrogate model, and the output layer has 140 neurons representing the time series output. The number of hidden layers (Fig. 7) is defined as two, with N_2 and N_3 neurons at the first and second hidden layers.

To train the surrogate model, the FE model is extensively simulated with properties sampled from bounded uniform distributions $E_1 \sim \mathcal{U}(54, 66)$ [MPa] and $G_{12} \sim \mathcal{U}(8.5, 11.5)$ [MPa] to generate 1024 samples. These bounds encompass the deterministic optimal values and offer sufficient margin to accommodate variations in the physical properties with temperature. During training rounds, data are divided with a

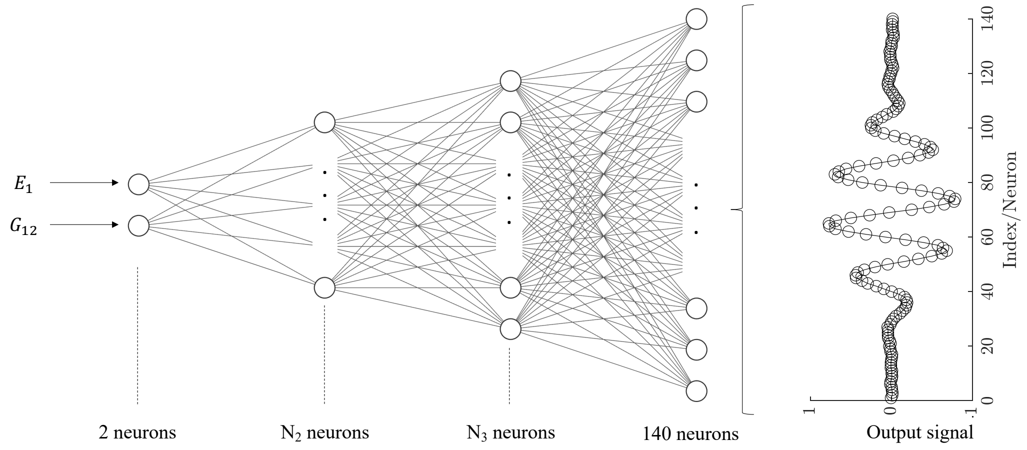

Figure 7: Surogate model architecture

proportion of 80/10/10, i.e., 820 samples for training, 102 for validation, and 102 for testing. The input parameters are normalized between 0 and 1, and the output signal is normalized between -1 and 1 to improve convergence. The model signal is truncated after the first wave package to reduce training time and the amount of data needed for network convergence. This package has a group speed of 5920 m/s, within the range expected for the first symmetric mode of a carbon/epoxy composite in frequency/thickness tested [8], and the second package consists of its border reflection. Figure 8a-c shows the distribution of the sampling space population.

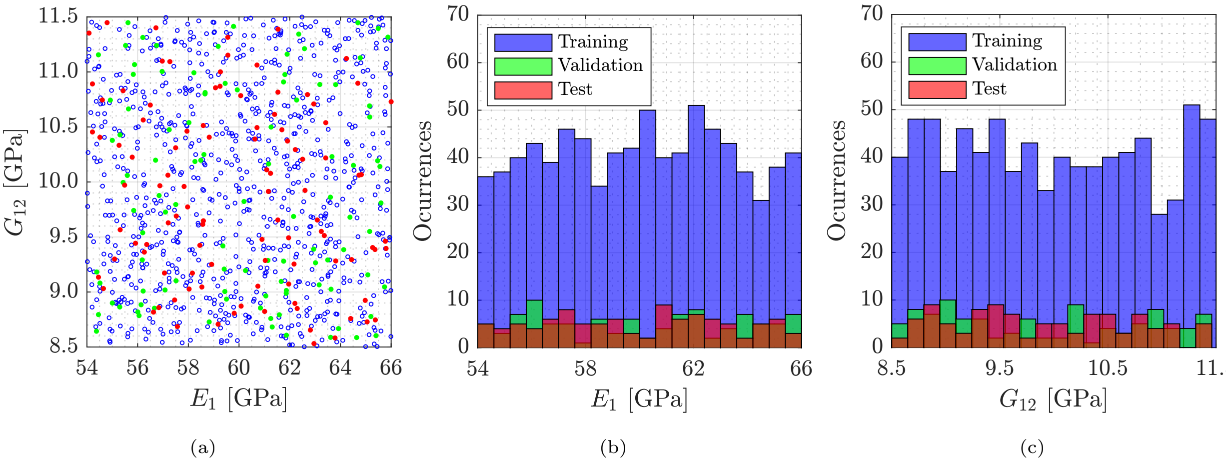

(a) (b) (c)

Figure 8: Training (🟦), validation (🟩), and test (🟥) data distribution. (a) 2D dispersion; (b) E_1 Histogram; and (c) G_{12} Histogram

The surrogate model is trained using the Stochastic Gradient Descent with Momentum (SGDM) algorithm, and the network loss on validation data is employed as the stopping criterion for training. The discrepancy between the output of the surrogate model and the full-order FE model is the error metric guiding the learning process. At regular intervals, the training algorithm assesses the validation data, and if the loss on the validation data ceases to decrease or begins to increase, the training process is halted.

The performance of the proposed surrogate model is influenced by its hyperparameters, such as the number of neurons in the hidden layers, activation functions, initial learning rate, and the amount of available training data. N_2 and N_3 are defined through an exploratory search within 50 to 300 neurons per layer. Figure 9 presents the root mean square error (RMSE) concerning the number of neurons in the second and third layers. The RMSE is not significantly influenced by N_2, remaining stable with 50 or more neurons. In contrast, the number of neurons N_3 has a greater influence on the RMSE, with the error stabilizing with 200 or more neurons. Therefore, an architecture with 50 neurons for N_2 and 200 neurons for N_3 is defined.

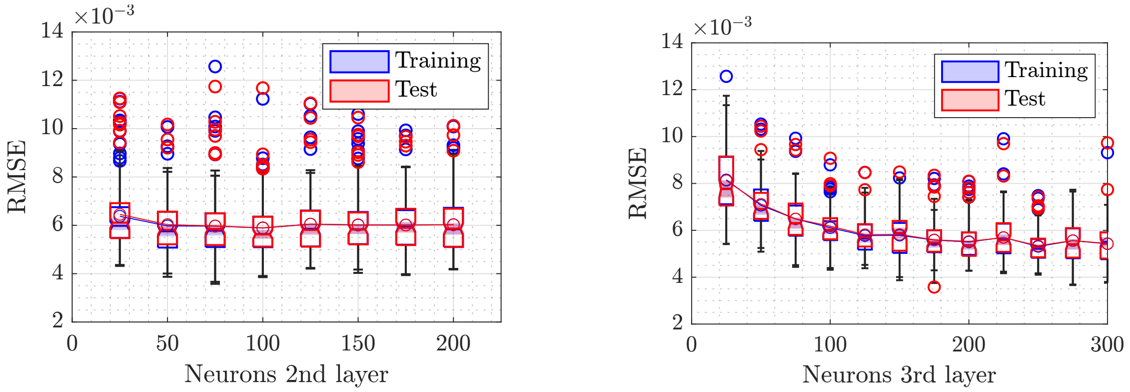

(a)

(b)

Figure 9: Training (🟦) and test (🟥) RSME as a function of the number of neurons on (a) the second layer; and (b) third layer

The training process is repeated with varying sample sizes to evaluate the network's convergence regarding the training data. Figure 10 demonstrate that the RMSE decreases on both the training and test data as the number of training samples increases and eventually converges. Additionally, note that approximately 500 samples are the minimum required for the surrogate model to converge, i.e., less than the 820 samples used.

Figure 11 presents the results from the surrogate model compared to the FE model in three values of E_1 and G_{12} randomly selected from the test data. In these three samples, the surrogate model's response replicated the FE model's response without noticeable differences. Additional tests showed that this behavior is repeated throughout the entire training range.

In summary, the main advantages of the surrogate model are (i) its computation speed and (ii) the possibility of parallelizing the data-gathering step across multiple computers. For instance, each simulation using the FE model takes two to three minutes on a typical PC with an Intel core i7 CPU (3,0 MHz and

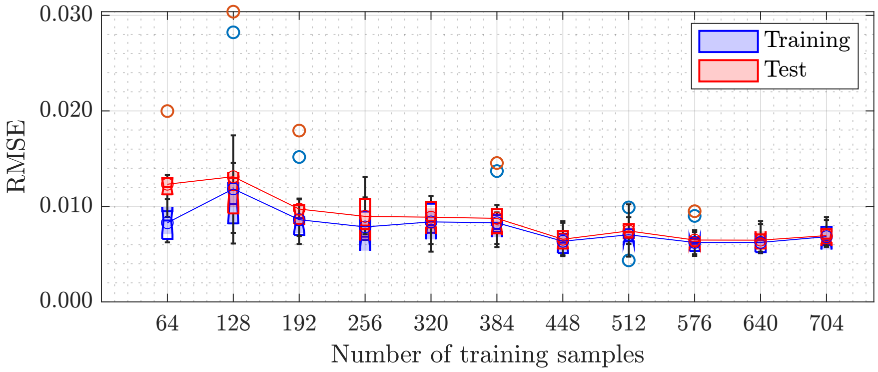

Figure 10: Training (🟦) and test (🟥) RSME with varying amounts of training samples

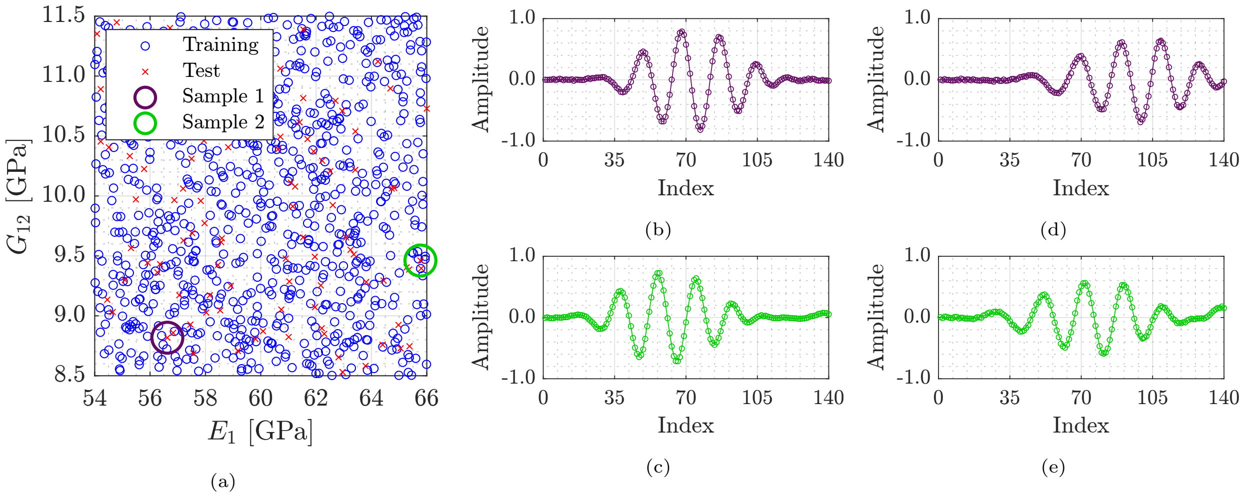

(a)

(b)

(c)

(d)

(e)

Figure 11: Results for surrogate model performance on test data compared to FE model. (a) Subspace of surrogate model training and test data with two randomly selected test samples highlighted for model evaluation; (b) and (c) represents PZT 2 signals for samples 1 and 2, respectively; (d) and (e) represents PZT 3 signals for samples 1 and 2, respectively. On signal graphs (b) to (e), full lines (▬) represent FE model predictions and circles (∘) represent ANN model results for the same sampled properties

4 cores) and 16 GB of RAM, whereas the surrogate model takes less than a second to evaluate. The 1024 simulations used at the training step took around 30 hours to perform (without a parallelization scheme). After training, the surrogate model can be used for interpolation purposes within the domain defined for E_1 and G_{12}. In the current application, the same surrogate model can be used for all MCMC rounds at the temperature interval from 0°C to 60°C, reducing exponentially the amount of simulations and time required for the Bayesian inference process.

4.2.3. Bayesian updating

- *E_1 and G_{12} updating for 20°C*

The framework for stochastic updating proposed in section 2.2.2 is first applied to the experimental data collected at 20°C. The updating procedure is conducted using FE and surrogate models in this particular temperature condition. The outcomes of the two approaches are then compared, taking into account the random walk performance and the updated posterior probability density function (PDF). This comparison uses the surrogate model to assess the uncertainty introduced in the Bayesian inference process.

The prior probability distributions for the variables $\Theta = \{E_1, G_{12}\}^T$ are defined as $E_1 \sim \mathcal{U}(54, 66)$ [MPa] and $G_{12} \sim \mathcal{U}(8.5, 11.5)$ [MPa] to contain the optimal values obtained in the deterministic fitting and allow a search range for the random walk algorithm. The initial value for each parameter is defined as the center of the search range $\Theta_i = \{60, 10\}^T$. For the Markov Chain estimation, the variance of the likelihood function is defined iteratively through rounds of the fitting algorithm, trying to ensure a stable acceptance rate between 40 and 50%. As can be observed in Fig. 12, the behavior of the FE and surrogate models is similar throughout the evolution of the Markov chain.

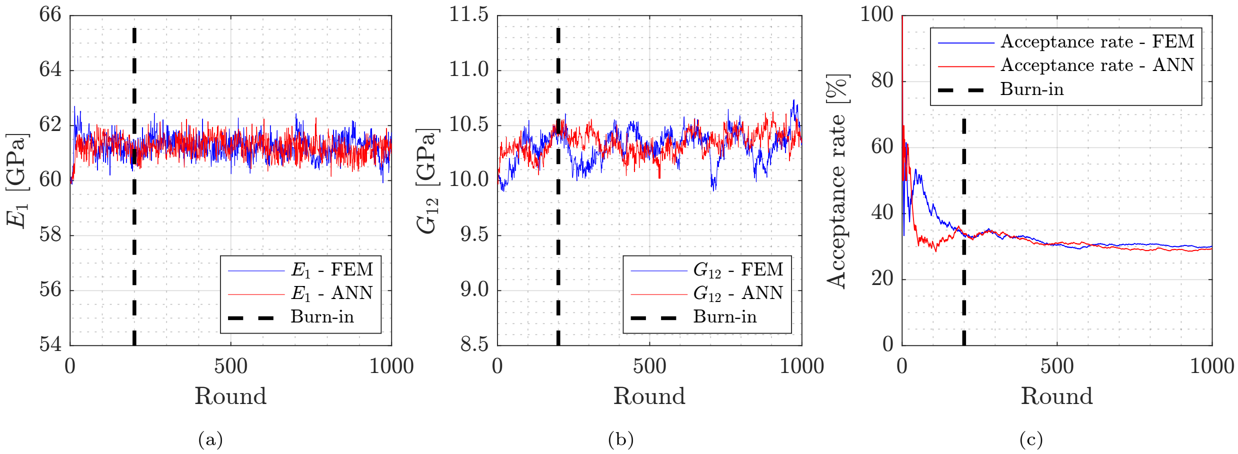

(a) (b) (c)

Figure 12: Comparison between the random-walk performance of the MCMC algorithm while searching for E_1 and G_{12} using the FE and surrogate models at 20°C. (a) Random walk values for E_1; (b) random walk values for G_{12}; and (c) acceptance rate for each strategy.

The random walk starts at the center of the search space for each parameter, and the Metropolis-Hastings sampling algorithm generates a new set of samples iteratively by proposing slight changes to the current set. Following the Metropolis-Hastings acceptance criteria, the proposed samples are accepted or rejected based on their likelihood compared to the current values. After several iterations, and upon proper adjustment of the MCMC parameters such as variance and step size for each round, the algorithm converges to an optimal region. This convergence is clearly illustrated in Figs. 12a and 12b. The algorithm continues to sample from the posterior distribution within this stability region. In instances where the algorithm deviates significantly from the optimal region for the parameters, the proposed values become less likely to belong to the posterior distribution. As a result, the Metropolis-Hastings sampling algorithm tends to return to the region where it is more likely to acquire valuable information. The initial portion of the samples, which may exhibit transient behavior, can be discarded through a process known as "burn-in." This study sets the burn-in at 20% based on the acceptance rate curve presented in Fig. 12c. Figure 13 compares the posterior PDFs sampled for E_1 and G_{12} using the Metropolis-Hastings algorithm.

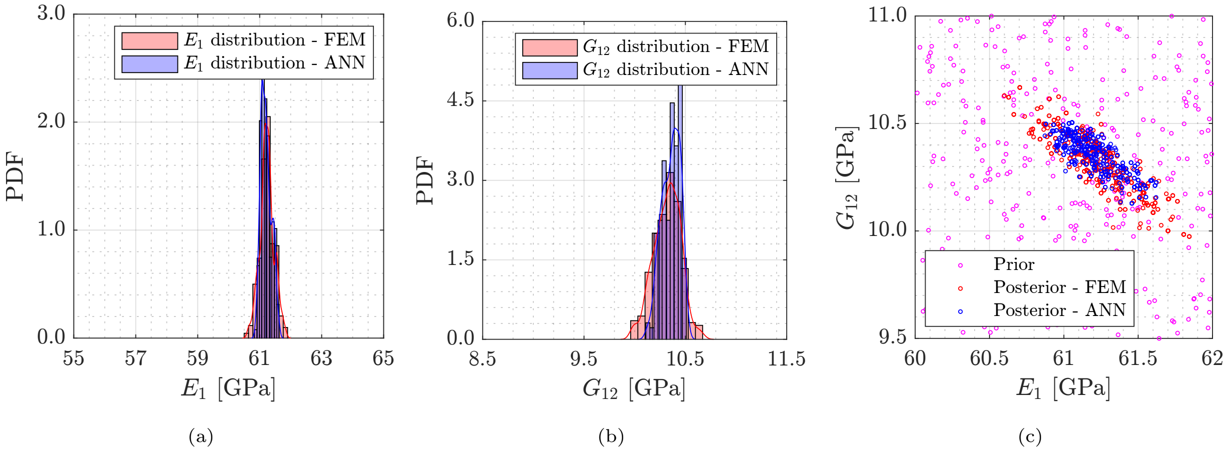

Figure 13: Comparison between distributions obtained using the FE and surrogate models at 20°C. (a) *A posteriori* for E_1; (b) *a posteriori* for G_{12}; and (c) two dimensional *a priori* and *a posteriori* distributions

The FE and surrogate models are evaluated using the values within the 99% confidence interval as depicted in the histograms in Figs. 13a and 13b. This procedure yields the confidence interval for the output of the models. Figure 14 illustrates the confidence intervals for the signals obtained from the surrogate model. Observations reveal that the confidence interval for the signal measured at PZT-2 is narrower than that of PZT-3. This phenomenon can be attributed to the greater dispersion observed in the data obtained from PZT-3, as shown in Fig. 3 along with a lower signal-to-noise ratio.

Table 2 summarizes the results. Note that the surrogate model does not introduce significant differences in the Bayesian inference process when compared to the results obtained from the FE model. In addition to the results being similar, the proposed framework using the surrogate model is computationally efficient and significantly reduces the time required for analyzing the Markov chains. A complete Markov-chain Monte Carlo round with 1000 samples takes at least 32 hours using the FE model, excluding the initial parameter tuning phase. In contrast, the same algorithm with the surrogate model takes about 240 s, i.e., almost 500 times less than the FE model. Moreover, the surrogate model facilitates simulations of longer chains, leading to increased points collected from the posterior probability distribution and enabling multiple tests to evaluate the convergence of the method. The surrogate model introduces a main computational cost related to the data required for training. However, this expense can be efficiently addressed by distributing

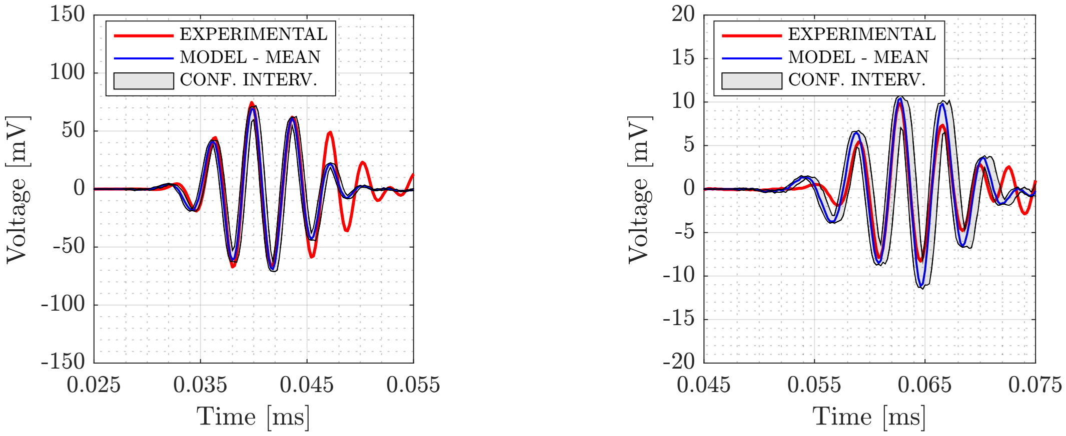

(a) (b)

Figure 14: Experimental (—), ANN model mean (—), and model confidence interval (■) signal Comparison for 20°C. (a) PZT 2; and (b) PZT 3

the training simulations across multiple machines, thus reducing the overall time required. In contrast, traditional MCMC simulations must be performed sequentially due to the sequential dependency of each chain step.

Table 2: Mechanical parameters obtained for 20°C

		Model	
		FE	ANN
	Mean	61.25	61.24
	Standard deviation	0.29	0.23
E_1 [GPa]	Coefficient of variation (CV)	0.47	0.37
	1% Percentile	60.26	60.10
	99% Percentile	61.97	61.62
	Mean	10.29	10.32
	Variance	0.14	0.09
G_{12} [GPa]	Coefficient of variation (CV)	1.41	0.9
	1% Percentile	9.92	10.11
	99% Percentile	10.52	10.47
	Time (s)	115000	240

- *E_1 and G_{12} updating from 0°C to 60°C*

The same strategy used for 20°C is applied to fit the FE model to the experimental data collected at temperatures from 0 to 60°C. However, these adjustments are only made using the surrogate model. The Markov chain parameters are selected at each temperature to maintain an acceptance rate after convergence of the algorithm between 30% and 50% at the end of approximately 4000 simulations. This is possible with the surrogate model since each 1000 MCMC takes around 3 to 4 minutes. Table 3 presents the results for E_1 and G_{12}, and Fig. 15 shows the sampled posterior distributions.

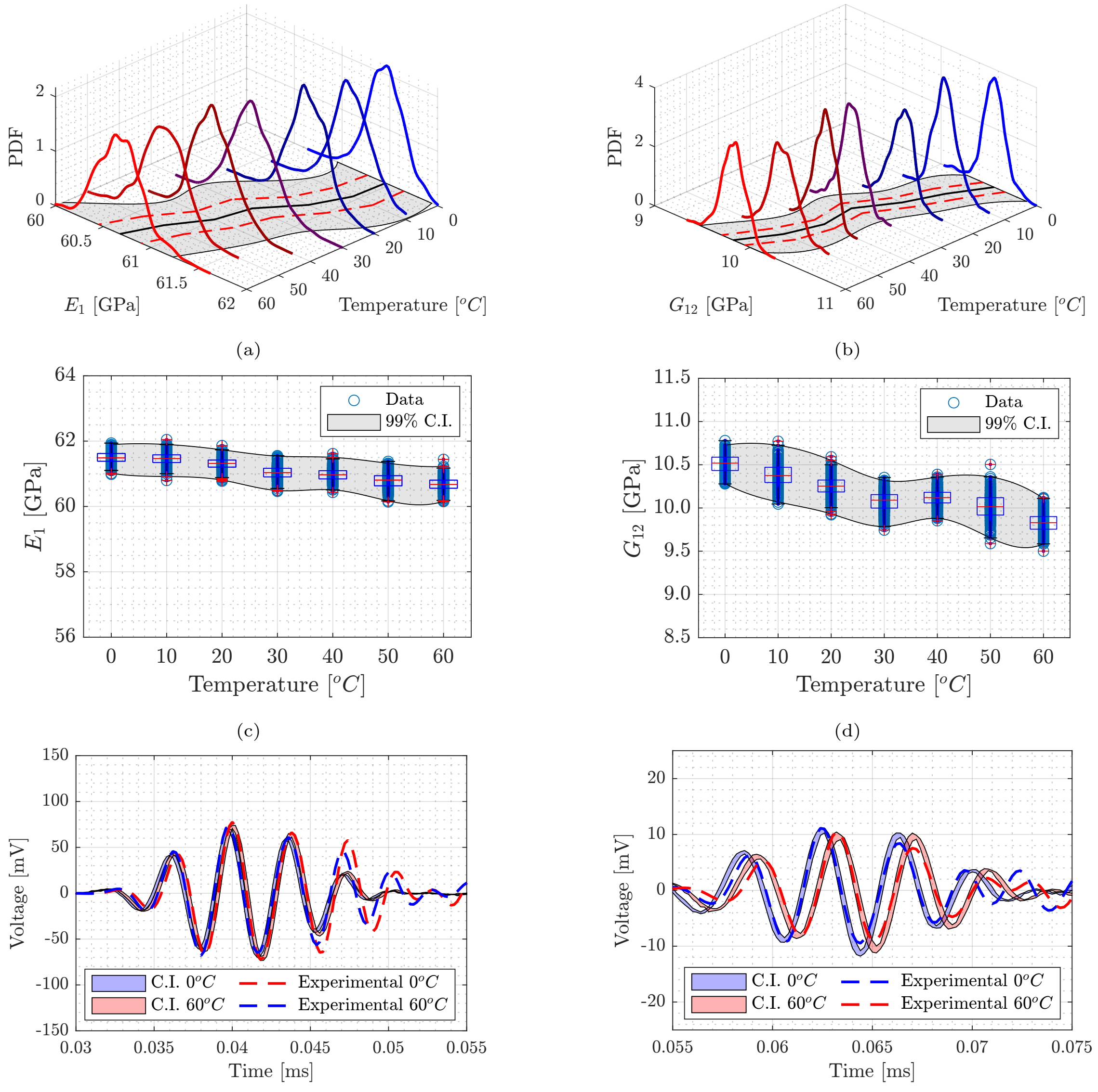

(a) (b)

(c) (d)

(e) (f)

Figure 15: Confidence intervals for probability density functions of E_1 and G_{12} with temperature. (a) 3D distribution for E_1; (b) 3D distribution for G_{12}; (c) 2D distribution for E_1; (d) 2D distribution for G_{12}; (e) experimental results (- -) and confidence intervals (■) for signal of PZT 2; and (f) experimental results (- -) and confidence intervals (■) for signal of PZT 3. C.I. represents the confidence intervals.

Table 3: Mechanical parameters obtained for temperature range from 0°C to 60°C

		0°C	10°C	20°C	30°C	40°C	50°C	60°C
E_1	Mean	61.46	61.44	61.30	61.06	61.00	60.80	60.67
	Standard deviation	0.191	0.207	0.190	0.215	0.195	0.214	0.225
	Coefficient of variation (CV)	0.310	0.337	0.310	0.352	0.320	0.351	0.371
	1% Percentile	60.94	60.91	60.82	60.55	60.57	60.20	60.08
	99% Percentile	61.98	61.05	61.83	61.67	61.51	61.34	60.32
G_{12}	Mean	10.56	10.38	10.26	10.06	10.11	10.01	9.82
	Standard deviation	0.116	0.124	0.108	0.114	0.103	0.131	0.121
	Coefficient of variation (CV)	1.09	1.19	1.05	1.14	1.02	1.30	1.23
	1% Percentile	10.14	10.06	10.01	9.74	9.84	9.70	9.50
	99% Percentile	10.87	10.69	10.55	10.38	10.32	10.40	10.11

It is possible to notice a trend of reduction of material stiffness with increasing temperature, which is consistent with the behavior of a carbon/epoxy laminate. The trend of the mean results is mostly linear, as can be observed in Figs. 15c and 15d. The material's elastic modulus starts at 61.46 GPa at 0°C and decreases with temperature to reach the value of 60.67 GPa at 60°C, i.e., a variation of 1.3%. The shear modulus presents the same trend, from 10.56 GPa to 9.82 GPa, with a variation of 7.0%. The higher reduction on the shear module can be explained by the viscoelastic nature of the epoxy resin, which is not present in the carbon fiber. This larger variation for the values of G_{12} compared to E_1 results in a greater dispersion of the signals for PZT3, which, located 45 degrees from the excitation point, is more affected by the material's shear modulus.

The only exception to the observed trend in Figs. 15c and 15d is the value of G_{12} at a temperature of 30°C, which appears as an outlier, displaying a lower value than that obtained at 40°C. To investigate this anomaly, the measured signals for PZT-2 were analyzed concerning temperature variations. Figure 16 shows a zoom near the peak of the first wave package from Fig. 3(c). The wave signals exhibited a consistent trend of delay with temperature increase, except for the measurement at 30°C, which deviated from the expected trend. Subsequent investigation into the experimental setup indicated a potential issue with the temperature controller in the thermal chamber on the day of the experiment. The ambient temperature fluctuated above 30°C, and the ON-OFF control logic of the controller faced challenges in maintaining an exact internal atmosphere of 30°C. Despite this experimental anomaly, the proposed fitting framework demonstrated robustness. It effectively captured the temperature trend in the experimental data and accurately reflected it in the FE model.

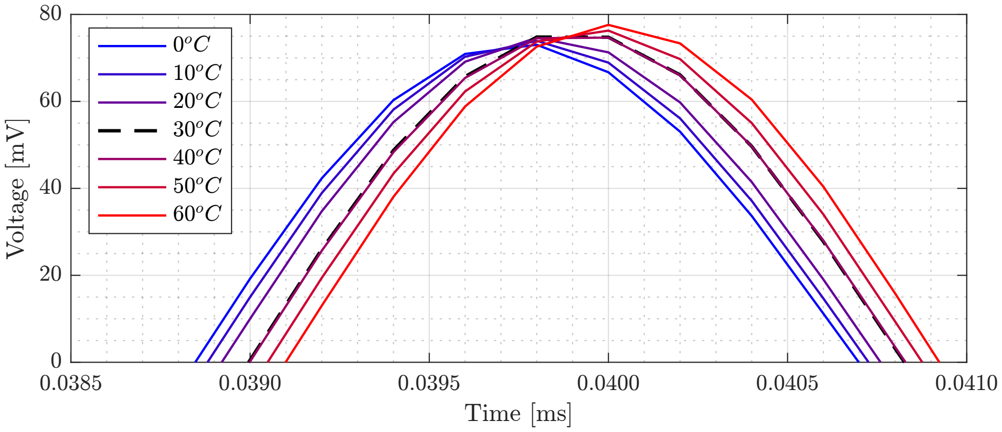

Figure 16: Close-up of the experimental signal wave peaks from PZT-2 in the temperature range of 0°C to 60°C

5. Conclusions

This paper presents a framework that addresses the critical challenge of incorporating temperature effects in Lamb wave simulations within composite structures, in the context of SHM applications. A stochastic FE model capable of accurately simulating Lamb wave behavior under varying temperature was successfully developed through Bayesian inference.

A three-step process was employed in the framework: (i) initial adjustment, followed by a (ii) Sobol sensitivity analysis, and (iii) a stochastic adjustment through Bayesian inference and MCMC simulations. This framework has demonstrated its effectiveness in calibrating the FE model by considering uncertainties in relevant mechanical parameters of the composite plate's fiber/resin system. The model results are generated within a confidence interval that align closely with experimental data.

Incorporating temperature effects is a critical consideration while developing reliable SHM systems based on Lamb waves due to their sensitivity to environmental conditions. The proposed framework was capable of producing a FE model that simulates Lamb wave signals from 0 to 60 °C with the experimental dispersion.

An additional contribution of this work lies in introducing a machine learning-based surrogate model within the Bayesian inference process. Leveraging the capacity of neural networks, the surrogate model significantly reduces the time required for MCMC rounds, thereby accelerating the posterior distribution sampling process. In the demonstration case, the time required for the MCMC rounds reduced from, approximately, 30 hours using the classical FE model-based approach, to less than 5 minutes when using the surrogate model approach. This time reduction is achieved without compromising the FE model's accuracy, ensuring the reliability of the results.

The integration of Bayesian inference and a machine learning surrogate model for model updating brings us one step closer to practical SHM implementations for composite materials. The proposed framework provides a solid foundation for reliable and accurate simulations and paves the way for constructing a robust

SHM system suitable for practical, real-world implementation.

CRediT authorship contribution statement

Leonardo Ferreira: Writing - original draft & editing, software curation, visualization, investigation, validation. **Rafael Teloli:** Software curation, formal analysis, supervision, writing - review & editing. **Samuel da Silva:** Experimental setup design, experimental tests, conceptualization, writing - original draft, investigation, formal analysis, project administration. **Eloi Figueiredo:** Writing - review & editing, formal investigation. **Ionut Dragos:** Software, writing - review & editing, formal investigation. **Nuno Maia:** writing - review & editing, formal investigation, project administration. **Carlos Cimini:** Writing - review & editing, formal investigation, supervision.

Declaration of Competing Interest

The authors declare that they have no known competing financial interests or personal relationships that could have appeared to influence the work reported in this paper.

Acknowledgments

The authors thank the financial support provided by Coordenação de Aperfeiçoamento de Pessoal de Nível Superior (CAPES/Brazil)-Finance Code 001 and CAPES/FCT grant number 2019.00164.CBM and The Portuguese National Funding Agency for Science Research and Technology (FCT/Portugal) for promoting the collaboration between Brazil/Portugal. Leonardo Ferreira acknowledges the funding from CAPES/Brazil grant number and 88887.647575/2021-00. Samuel da Silva is thankful for the Brazilian National Council of Technological and Scientific Development (CNPq) grant number 306526/2019-0 and the São Paulo Research Foundation (FAPESP) grant number 19/19684-3. Eloi Figueiredo acknowledges the funding from FCT/Portugal through grant UIDB/ 04625/2020. Nuno Maia acknowledges the support of FCT/Portugal, through IDMEC, under LAETA, project UIDB/50022/2020. Carlos Cimini acknowledges the Fundação de Amparo à Pesquisa do Estado de Minas Gerais (Fapemig), the CNPq and the CAPES/Brazil for research support.

Data availability

The experimental data required to reproduce these findings are available to download from `https://github.com/shm-unesp/DATASET_PLATEUN01`.

References

[1] D. Wang, J. He, X. Guan, J. Yang, W. Zhang, A model assessment method for predicting structural fatigue life using Lamb waves, Ultrasonics 84 (2018) 319–328. `doi:10.1016/J.ULTRAS.2017.11.017`.

[2] P. B. Nagy, F. Simonetti, G. Instanes, Corrosion and erosion monitoring in plates and pipes using constant group velocity Lamb wave inspection, Ultrasonics 54 (7) (2014) 1832–1841. `doi:https://doi.org/10.1016/j.ultras.2014.01.017`.
URL `https://www.sciencedirect.com/science/article/pii/S0041624X14000183`

[3] T. Tong, J. Hua, J. Lin, H. Zhang, Disbond contours evaluation in aluminum/CFRP adhesive joint based on excitation recovery of Lamb waves, Composite Structures 294 (2022) 115736. `doi:https://doi.org/10.1016/j.compstruct.2022.115736`.
URL `https://www.sciencedirect.com/science/article/pii/S0263822322005128`

[4] C. Boller, G. R. Tomlinson, W. J. Staszewski (Eds.), Health monitoring of aerospace structures : smart sensor technologies and signal processing, J. Wiley, Chichester, West Sussex, England ; Hoboken, NJ, 2004.
URL `https://onlinelibrary.wiley.com/doi/book/10.1002/0470092866`

[5] X. Zeng, X. Liu, J. Yan, Y. Yu, B. Zhao, X. Qing, Lamb wave-based damage localization and quantification algorithms for CFRP composite structures, Composite Structures 295 (2022) 115849. `doi:10.1016/J.COMPSTRUCT.2022.115849`.

[6] G. Konstantinidis, B. W. Drinkwater, P. D. Wilcox, The temperature stability of guided wave structural health monitoring systems, Smart Materials and Structures 15 (4) (2006) 967. `doi:10.1088/0964-1726/15/4/010`.
URL `https://dx.doi.org/10.1088/0964-1726/15/4/010`

[7] F. L. di Scalea, S. Salamone, Temperature effects in ultrasonic lamb wave structural health monitoring systems, The Journal of the Acoustical Society of America 124 (2008) 161–174, doi: 10.1121/1.2932071. `doi:10.1121/1.2932071`.
URL `https://doi.org/10.1121/1.2932071`

[8] L. Wang, F. G. Yuan, Group velocity and characteristic wave curves of Lamb waves in composites: Modeling and experiments, Composites Science and Technology 67 (2007) 1370–1384. `doi:10.1016/J.COMPSCITECH.2006.09.023`.

[9] M. Mitra, S. Gopalakrishnan, Guided wave based structural health monitoring: A review, Smart Materials and Structures 25 (5) (2016) 053001. `doi:10.1088/0964-1726/25/5/053001`.
URL `https://dx.doi.org/10.1088/0964-1726/25/5/053001`

[10] A. D. Luca, D. Perfetto, A. D. Fenza, G. Petrone, F. Caputo, Guided wave SHM system for damage detection in complex composite structure, Theoretical and Applied Fracture Mechanics 105. `doi:10.1016/J.TAFMEC.2019.102408`.

[11] S. Ereiz, I. Duvnjak, J. F. Jiménez-Alonso, Review of finite element model updating methods for structural applications, Structures 41 (2022) 684–723. `doi:10.1016/J.ISTRUC.2022.05.041`.

[12] E. Simoen, G. D. Roeck, G. Lombaert, Dealing with uncertainty in model updating for damage assessment: A review, Mechanical Systems and Signal Processing 56-57 (2015) 123–149. `doi:https://doi.org/10.1016/j.ymssp.2014.11.001`.
URL `https://www.sciencedirect.com/science/article/pii/S0888327014004130`

[13] R. de O. Teloli, S. da Silva, T. G. Ritto, G. Chevallier, Bayesian model identification of higher-order frequency response functions for structures assembled by bolted joints, Mechanical Systems and Signal Processing 151. `doi:10.1016/J.YMSSP.2020.107333`.

[14] L. P. Miguel, R. O. Teloli, S. da Silva, Bayesian model identification through Harmonic Balance Method for hysteresis prediction in bolted joints, Nonlinear Dynamics 107 (1) (2022) 77–98. `doi:https://doi.org/10.1007/s11071-021-06967-2`.

[15] T. G. Ritto, R. Sampaio, R. R. Aguiar, Uncertain boundary condition bayesian identification from experimental data: A case study on a cantilever beam, Mechanical Systems and Signal Processing 68-69 (2016) 176–188. `doi:10.1016/J.YMSSP.2015.08.010`.

[16] X. Wang, T. L. Hill, S. A. Neild, A. D. Shaw, H. H. Khodaparast, M. I. Friswell, Model updating strategy for structures

with localised nonlinearities using frequency response measurements, Mechanical Systems and Signal Processing 100 (2018) 940–961. `doi:10.1016/J.YMSSP.2017.08.004`.

[17] A. Gallina, L. Ambrozinski, P. Packo, L. Pieczonka, T. Uhl, W. J. Staszewski, Bayesian parameter identification of orthotropic composite materials using lamb waves dispersion curves measurement, Journal of Vibration and Control 23 (2017) 2656–2671. `doi:10.1177/1077546315619264`.
URL `https://doi.org/10.1177/1077546315619264`

[18] W. J. Yan, D. Chronopoulos, S. Cantero-Chinchilla, K. V. Yuen, C. Papadimitriou, A fast Bayesian inference scheme for identification of local structural properties of layered composites based on wave and finite element-assisted metamodeling strategy and ultrasound measurements, Mechanical Systems and Signal Processing 143. `doi:10.1016/J.YMSSP.2020.106802`.

[19] H.-P. Wan, Z. Mao, M. D. Todd, W.-X. Ren, Analytical uncertainty quantification for modal frequencies with structural parameter uncertainty using a gaussian process metamodel, Engineering Structures 75 (2014) 577–589. `doi:https://doi.org/10.1016/j.engstruct.2014.06.028`.
URL `https://www.sciencedirect.com/science/article/pii/S0141029614003848`

[20] H.-P. Wan, W.-X. Ren, Stochastic model updating utilizing bayesian approach and gaussian process model, Mechanical Systems and Signal Processing 70-71 (2016) 245–268. `doi:https://doi.org/10.1016/j.ymssp.2015.08.011`.
URL `https://www.sciencedirect.com/science/article/pii/S0888327015003726`

[21] Z. Liu, D. Lesselier, B. Sudret, J. Wiart, Surrogate modeling based on resampled polynomial chaos expansions, Reliability Engineering & System Safety 202 (2020) 107008. `doi:https://doi.org/10.1016/j.ress.2020.107008`.
URL `https://www.sciencedirect.com/science/article/pii/S0951832020305093`

[22] H. Lim, L. Manuel, Distribution-free polynomial chaos expansion surrogate models for efficient structural reliability analysis, Reliability Engineering & System Safety 205 (2021) 107256. `doi:https://doi.org/10.1016/j.ress.2020.107256`.
URL `https://www.sciencedirect.com/science/article/pii/S0951832020307560`

[23] L. Zhou, L. Wang, L. Chen, J. Ou, Structural finite element model updating by using response surfaces and radial basis functions, Advances in Structural Engineering 19 (2016) 1446–1462. `doi:10.1177/1369433216643876`.
URL `https://doi.org/10.1177/1369433216643876`

[24] M. A. Fakih, M. Chiachío, J. Chiachío, S. Mustapha, A Bayesian approach for damage assessment in welded structures using Lamb-wave surrogate models and minimal sensing, NDT and E International 128. `doi:10.1016/J.NDTEINT.2022.102626`.

[25] K. H. Padil, N. Bakhary, H. Hao, The use of a non-probabilistic artificial neural network to consider uncertainties in vibration-based-damage detection, Mechanical Systems and Signal Processing 83 (2017) 194–209. `doi:https://doi.org/10.1016/j.ymssp.2016.06.007`.
URL `https://www.sciencedirect.com/science/article/pii/S0888327016301893`

[26] A. Lye, A. Cicirello, E. Patelli, Sampling methods for solving Bayesian model updating problems: A tutorial, Mechanical Systems and Signal Processing 159 (2021) 107760. `doi:https://doi.org/10.1016/j.ymssp.2021.107760`.
URL `https://www.sciencedirect.com/science/article/pii/S0888327021001552`

[27] S. da Silva, J. Paixão, M. Rébillat, N. Mechbal, Extrapolation of ar models using cubic splines for damage progression evaluation in composite structures, Journal of Intelligent Material Systems and Structures 32 (2020) 284–295, doi: 10.1177/1045389X20963171. `doi:10.1177/1045389X20963171`.
URL `https://doi.org/10.1177/1045389X20963171`

[28] M. A. Bud, I. Moldovan, L. Radu, M. Nedelcu, E. Figueiredo, Reliability of probabilistic numerical data for training machine learning algorithms to detect damage in bridges, Structural Control and Health Monitoring 29 (7) (2022) e2950. `arXiv:https://onlinelibrary.wiley.com/doi/pdf/10.1002/stc.2950`, `doi:https://doi.org/10.1002/stc.2950`.
URL `https://onlinelibrary.wiley.com/doi/abs/10.1002/stc.2950`

[29] S. S. Jin, H. Ju, H. J. Jung, Adaptive Markov chain Monte Carlo algorithms for Bayesian inference: recent advances and comparative study, https://doi.org/10.1080/15732479.2019.1628077 15 (2019) 1548–1565. doi:10.1080/15732479.2019.1628077.

URL https://www.tandfonline.com/doi/abs/10.1080/15732479.2019.1628077

[30] R. da S Raqueti, R. de O Teloli, S. da Silva, P. Bussetta, J. Americo Cunha, On the use of stochastic Bouc–Wen model for simulating viscoelastic internal variables from a finite element approximation of steady-rolling tire, Journal of Vibration and Control 0 (0) (0) 10775463221125038. arXiv:https://doi.org/10.1177/10775463221125038, doi:10.1177/10775463221125038.

URL https://doi.org/10.1177/10775463221125038

[31] A. Saltelli, M. Ratto, T. Andres, F. Campolongo, J. Cariboni, D. Gatelli, M. Saisana, S. Tarantola, Global sensitivity analysis: the primer, John Wiley & Sons, 2008.

[32] S. Marelli, B. Sudret, UQLab: A framework for uncertainty quantification in Matlab, in: Vulnerability, Uncertainty, and Risk, ASCE Reston, VA, 2014, pp. 2554–2563. arXiv:https://ascelibrary.org/doi/pdf/10.1061/9780784413609.257, doi:10.1061/9780784413609.257.

URL https://ascelibrary.org/doi/abs/10.1061/9780784413609.257

[33] A. d. A. França, Detecção e localização de danos em materiais compósitos aplicado em aeronaves utilizando redes neurais artificiais, Ph.D. thesis, Universidade Estadual Paulista (Unesp) (2014).

[34] F. Moser, L. J. Jacobs, J. Qu, Modeling elastic wave propagation in waveguides with the finite element method, NDT and E International 32 (1999) 225–234. doi:10.1016/S0963-8695(98)00045-0.

[35] M. Gresil, V. Giurgiutiu, Y. Shen, B. Poddar, Guidelines for using the finite element method for modeling of guided Lamb wave propagation in shm processes, e-Journal of Nondestructive Testing (eJNDT) 1435-4934.

URL https://www.ndt.net/search/docs.php3?id=14011

[36] J. Sirohi, I. Chopra, Fundamental understanding of piezoelectric strain sensors, Journal of Intelligent Material Systems and Structures 11 (4) (2000) 246–257. arXiv:https://doi.org/10.1106/8BFB-GC8P-XQ47-YCQ0, doi:10.1106/8BFB-GC8P-XQ47-YCQ0.

URL https://doi.org/10.1106/8BFB-GC8P-XQ47-YCQ0

[37] Composite materials handbook, SAE International on behalf of CMH-17, a division of Wichita State University, 2017.

[38] J. M. F. d. Paiva, S. Mayer, M. C. Rezende, Comparison of tensile strength of different carbon fabric reinforced epoxy composites, Materials Research 9 (Mat. Res., 2006 9(1)). doi:10.1590/S1516-14392006000100016.

URL https://doi.org/10.1590/S1516-14392006000100016